NJC

PAPER

View Article Online
View Journal

Cite this: DOI: 10.1039/d5nj03499j

A vanadium atom sandwiched by boron nitride and graphene sheets for electrochemical reduction of nitric oxide: insights from first-principles calculations

Osamah Abdulbari Khadhair,[a] R. Roopashree,[b] Helen Merina Albert,[c] Subhashree Ray,[d] Renu Sharma,[e] Saodatkhon Ibragimova,[fg] Akmal Abilkasimov,[h] Abdusalom Umarov,[i] P. R. Jangir,[j] Mustafa Ahmed Diab*[kl] and Mumtaj Shah[m]

The electrochemical conversion of toxic nitric oxide (NO) into useful chemicals presents an auspicious approach for addressing environmental pollution. Designing effective and active catalysts for NO reduction is crucial and has significant potential for addressing environmental challenges. This study explores the effective role of a vanadium (V) atom situated between hexagonal BN and graphene nanosheets (BN/V/Gr) as an electrocatalyst for the NO electrochemical reduction, utilizing first-principles calculations. Our findings indicate that the BN/V/Gr electrocatalyst can greatly activate the NO molecule, promoting the production of ammonia (NH_3) and nitrogen (N_2) at low and high surface coverages, respectively. The catalyst shows remarkable catalytic activity for NO reduction, achieving a limiting potential of only 0.17 V for NH_3, and 0.53 V for N_2 formation. The enhanced catalytic activity of the proposed electrocatalyst can be attributed to the polarization field induced on the BN layer by the presence of the V atom. This polarization results in a significant accumulation of electron density on the adjacent B atom, effectively activating the adsorbed NO molecule. These insights provide valuable knowledge that could assist in the design of metal-free electrocatalysts, offering innovative solutions for removing toxic NO molecules from our atmosphere.

Received 31st August 2025,
Accepted 21st October 2025

DOI: 10.1039/d5nj03499j

rsc.li/njc

[a] Department of Biomedical Engineering, University of Warith Alanbiyaa, College of Engineering, Iraq
[b] Department of Chemistry and Biochemistry, JAIN (Deemed-to-be University), Bangalore, Karnataka, India
[c] Department of Physics, Sathyabama Institute of Science and Technology, Chennai, Tamil Nadu, India
[d] Department of Biochemistry, IMS and SUM Hospital, Siksha 'O' Anusandhan, Bhubaneswar, Odisha-751003, India
[e] Department of Chemistry, University Institute of Sciences, Chandigarh University, Mohali, Punjab, India
[f] University of Tashkent for Applied Sciences, Str. Gavhar 1, Tashkent 100149, Uzbekistan
[g] National Research University TIIAME, Kori Niyoziy 39, Tashkent 100000, Uzbekistan
[h] Kimyo International University in Tashkent, Shota Rustaveli Str. 156, Tashkent 100121, Uzbekistan
[i] University of Tashkent for Applied Sciences, Str. Gavhar 1, Tashkent 100149, Uzbekistan
[j] Sharda School of Engineering and Sciences, Sharda University, Knowledge Park III, Greater Noida, Uttar Pradesh-201310, India
[k] Medical Laboratory Technique College, The Islamic University, Najaf, Iraq
[l] Medical Laboratory Technique College, The Islamic University of Babylon, Babylon, Iraq
[m] Department of Chemical Engineering, College of Engineering, King Khalid University, Abha, 61141, Saudi Arabia

1. Introduction

A significant challenge the world faces today is the persistent rise in the levels of harmful air pollutants in the atmosphere.[1,2] Nitric oxide (NO) is a key environmental contaminant released from the combustion of fossil fuels in vehicle engines and industrial processes. Elevated levels of NO can contribute to various health issues in humans, including neurodegenerative diseases like Parkinson's[3,4] and Alzheimer's.[5] Another issue with NO is its possible interaction with water molecules present in the atmosphere, which can result in the formation of "acid rain." This acidic precipitation can adversely affect plants, soil, forests, human health, and buildings.[6] Consequently, it is crucial to find effective methods for the removal or reduction of NO. One of the most effective strategies is through the NO electrochemical reduction (NOER), which converts it into ammonia (NH_3) and nitrogen (N_2) under mild reaction conditions. Various transition metals (TM), such as copper (Cu), platinum (Pt), Rhodium (Rh), and palladium (Pd), are commonly used as catalyst.[7–10] These TMs have strong catalytic performance for NOER, but their limited availability, high costs, and poor long-term stability may restrict their use.

Therefore, finding high-efficiency, cost-effective, and metal-free alternatives for these electrocatalysts would be highly beneficial.

Single-atom catalysts (SACs) have emerged as a groundbreaking concept in the fields of chemistry and materials science.[11–14] Especially, TM-based SACs (TM-SACs) show significant promise for catalyzing the reduction of species such as N_2[15–18] and NO.[19–22] This is primarily attributed to the ''charge donation-backdonation'' mechanism that takes place between the d-orbitals of TM and the frontier molecular orbitals of the host material.[23–25] The ''chainmail''-protected catalyst concept,[19] proposed by Bao and colleagues, involves sandwiching a TM-SAC between two graphene sheets. The strong attraction between the TM atoms and the graphene sheets helps keep the metal atoms from moving around and clumping together. As a result, the TM atoms donate charge to the graphene, enhancing the electrocatalytic activity at the graphene surface. However, using graphene on its own is not the most effective approach. The C atoms in graphene are generally inert or chemically unreactive to function as effective catalytic centers. Additionally, the high conductivity of graphene tends to delocalize polarization charges, reducing their ability to accumulate and create a strong depolarization field. This depolarization field is crucial for the performance of catalysts in electrocatalytic reactions.[26] Consequently, this may lead to the screening of the induced electric field, which can adversely affect electrocatalytic processes. Ultimately, graphene has a diverse array of electronic states originating from the p-orbitals located near its Fermi level, enabling the formation of hybrid orbitals with the d-orbitals of TMs, which can influence the low-coordination characteristics of SACs. These properties are significant in enhancing the catalytic performance and selectivity of SACs, making them valuable in various chemical reactions.[27–29]

Nowadays, different nanomaterials have been used in medicine,[30,31] food packing,[32] diodes,[33] water purification,[34–36] gas sensing,[37,38] energy,[39] drug adsorption,[40,41] and so on. Hexagonal boron nitride (h-BN) is a 2D material that serves as a structural analogue to graphene.[42] It possesses exceptional physicochemical characteristics that make it ideal for incorporation into a SAC. These properties include excellent oxidation resistance, remarkable thermal stability, and a wide band gap, which contributes to its insulating nature.[43–46] In comparison, graphene is an intrinsically semi-metal with a zero band gap.[47] Despite this, graphene's exceptional ability to efficiently transfer energetic charges to TM-SACs through electrocatalysis can be combined with the advantages of h-BN. Specifically, h-BN contains boron (B) atoms that can serve as catalytic sites,[48,49] while its wide band gap results in poor coupling with TMs due to the lack of electronic states. This combination reduces the strong polarization electric field typically associated with TM-SACs, stabilizing it to a moderate level on the h-BN surface. For instance, experimental studies[50] have previously found that after immobilization on graphitic surfaces, h-BN exhibits a better electrochemical activity for the ORR. Zhong *et al.*[51] found that the AB stacking of the graphene/h-BN double-layer nanostructure is the most stable arrangement, and there is a linear relationship between the band gap and the stress of the structure. Therefore, an effective strategy to enhance catalytic performance in electrocatalysis involves utilizing the unique advantages of graphene, which is adept at efficiently transferring energetic charges, along with the abundant catalytic sites offered by h-BN.

Density functional theory (DFT) is currently an effective tool for exploring various catalytic aspects of electrochemical processes. The insights gained from DFT calculations play a crucial role in the rational fabrication of more effective catalytic materials, paving the way for the identification of new potential catalysts that can be verified through experimental work.[52–54] DFT is commonly employed to simulate a range of electrochemical reactions in either gas or solvent phases, enabling a detailed investigation of catalytic features and properties at the atomic level, including adsorption energies, Gibbs free energies, and activation barriers.[55] In DFT calculations, solvation effects can be handled through two primary methods: the explicit approach and the implicit approach.[56] The explicit method involves incorporating water molecules into the system to model the solvent environment, which may consist of several individual water molecules, one or two water bilayers, or even full solvation with multiple bilayers.[57,58] Although the explicit approach generally enhances the accuracy of vacuum calculations, the added water molecules or bilayers may not always accurately represent the true water structure at the solid–liquid interface. The explicit sampling of solvents remains computationally impractical, largely due to solvent–solvent interactions.[59,60] To address this issue, researchers often substitute the solvent with a dielectric medium designed to mimic the electrostatic characteristics of the electrolyte/metal interface. In recent decades, significant advancements have been made in enhancing implicit solvent models to effectively simulate solid–electrolyte interfaces, bringing their outcomes closer to those generated by traditional molecular dynamics (MD) simulations that use an implicit solvent.[61] However, a major limitation of implicit solvent models is their inability to accurately represent interactions between the solvent and solute or surface, as well as hydrogen bonding among water molecules.[62] Furthermore, it is widely recognized that the strength of electrostatic contributions is affected by pH-dependent surface charging.[63,64] The conductor-like screening model (COSMO),[65] which is based on quantum mechanics, modifies a general class of dielectric continuum solvation models and is often used to simulate the solvent environment (*e.g.*, water) in different electrochemical processes.[66] COSMO utilizes quantum chemical calculations to determine the surface charge densities of a molecule within a dielectric medium that resembles the solvent. This model also accounts for polarization effects due to the dielectric shielding of the electrolyte. Typically, the COSMO approximation closely matches the exact solution, particularly for strong dielectrics like water.[67,68]

Recently, an ultrathin sandwich catalyst was fabricated by integrating the chemical vapor deposition technique with the poly(methyl methacrylate) transfer method.[69] This innovative catalyst features iron (Fe) atoms nestled between a thin layer of h-BN and a graphene film. The findings revealed that this

structure not only effectively directs electron transfer towards the h-BN surface under applied voltage but also inhibits the hydrogen evolution reaction (HER) by establishing a neutral polarization electric field without exposing the metal. Furthermore, the researchers utilized DFT calculations to evaluate various SACs sandwiched between h-BN and graphene for their potential to catalyze the oxygen reduction reaction (ORR).[70] Tang *et al.*[71] demonstrated that a single TM atom situated between h-BN and graphene sheets (BN/TM/Gr) can function as an efficient SAC for electrochemically reducing N_2. Notably, the catalytic performance of these systems was closely linked to the polarization of the TM atom, with BN/Ti/Gr and BN/V/Gr emerging as effective catalysts due to their impressive stability, energy efficiency, and capability to mitigate the competing HER. Building on this groundwork, the current study focuses on the reduction of NO using the BN/V/Gr catalyst. It investigates the potential for activating NO and producing ammonia (NH_3) and nitrous oxide (N_2O) using this substrate configuration. Due to the interactions at the interfaces, the V atom contributes charge to the h-BN, creating a polarization field on this layer. Consequently, a significant charge accumulates on the B atom adjacent to the V atom, allowing it to act as catalytic sites for activating and reducing NO.

2. Theoretical aspects

First-principles computations were conducted using the PBE[72] functional with a double numerical plus polarization (DNP) basis set, as implemented in the DMol.[4,73] To account for dispersion effects, Grimme's DFT-D2[74] approach was applied. The convergence criteria were set at 0.005 Å for displacement, 0.001 Ha $Å^{-1}$ for force, and 10^{-6} Ha for total energy. A $5 \times 5 \times 1$ *k*-point sampling of the Monkhorst–Pack grid was applied for geometry relaxation, whereas a $10 \times 10 \times 1$ *k*-point grid for partial density of states (PDOS) analyses. A basis set cut-off of 4.6 Å was used in all calculations. $4 \times 4 \times 1$ supercells of h-BN and graphene sheets were employed to model the coverage of a single V atom to form a sandwich structure. A 20 Å vacuum gap was implemented in the *z*-direction to eliminate interactions between neighboring layers. The Hirshfeld[47] charge analysis was conducted to obtain charge transfer values. *Ab initio* MD simulations (AIMD) were performed using a canonical NVT ensemble, to explore the thermal stability of BN/V/Gr at a temperature of 500 K over a total duration of 2 ps, and a time step of 1 fs. The stability of the complexes formed between the adsorbates and the electrocatalyst was obtained by analyzing the adsorption energy (E_{ads}), defined as $E_{ads} = E_{com} - E_A - E_S$, where E_{com}, E_A, and E_S are the total energies of the formed complex, the adsorbate, and the substrate, respectively. An $E_{ads} < 0$ value signifies an exothermic adsorption.

Using the computational hydrogen electrode (CHE) model,[75] a comprehensive analysis of the free energy diagrams for the NOER was performed. The free energy associated with the proton-electron pair (H^+/e^-) was defined as that of half a molecule of hydrogen gas ($\frac{1}{2}$ $H_2(g)$), establishing a baseline for this investigation. For each fundamental step in the reaction process, the change in free energy (ΔG) was evaluated using eqn (1):

$$\Delta G = \Delta E - T\Delta S + \Delta E_{ZPE} + \Delta G_U + \Delta G_{pH} \quad (1)$$

In this equation, ΔE represents the electronic energy difference, which accounts for the energy variations between reactants and products at the electronic level. ΔS indicates the variation in entropies. ΔE_{ZPE} denotes the change in zero-point energy, reflecting the energy associated with the quantum mechanical ground state of the molecules involved. The term ΔG_U signifies the free energy change linked to the electrode potential (U), providing insight into the electrochemical behavior of the system. Moreover, the pH level of the electrolyte significantly impacts electrochemical reactions by affecting proton-coupled electron transfer and charge distributions at the interface. In the standard CHE model, the effect of pH is included as an energy correction term, given by $\Delta G_{pH} = k_B T \times pH \times \ln 10$, where k_B is Boltzmann's constant. However, when measuring the electrode potential against the reversible hydrogen electrode (RHE), the pH effect is automatically included in the Nernst equation ($E_{RHE} = E + 0.0592 \times pH$ at $T = 298$ K). This means the pH correction is effectively canceled out, leading conventional computational models to often overlook the pH effects when using the RHE scale.[76] To calculate ΔE_{ZPE} and ΔS accurately, vibrational frequencies were applied based on normal-mode analysis utilizing DFT calculations, which allowed for a precise understanding of molecular vibrations and their contributions to energy changes. The temperature (T) was maintained at room temperature, specifically 298.15 K, to ensure relevance to common experimental conditions. The necessary zero-point energies and entropies for each free molecule were sourced from the NIST database,[77] providing reliable data for the calculations. The limiting potential (U_L), which serves as a key indicator of the NOER activity in sandwich systems, was determined using the formula $U_L = -\Delta G_{max}/e$. To further refine the analysis, the COSMO[65] model was used, which accounted for solvent effects (water, dielectric constant = 78.54).

3. Results and discussion

3.1. BN/V/Gr electrocatalyst

To construct the BN/V/Gr heterostructure, a V atom is first placed on a hexagon of graphene, followed by stacking a h-BN layer over the V-decorated graphene in an AB configuration. This arrangement is found to be more stable than other possible configurations due to the strong bonds formed between the V atom and the neighboring C, N, and B atoms. Fig. 1a illustrates the sandwich-like structure of the BN/V/Gr heterostructure through side and top views. After optimizing the resulting structure, the distance between graphene and h-BN sheets measures approximately 3.30 Å. This indicates that the reaction species of NOER cannot penetrate the two layers through the edges. The incorporation of a V atom leads to a notable deformation of the h-BN surface, causing the adjacent B atoms to rise from the sheet by about 0.10 Å. As a result, the B

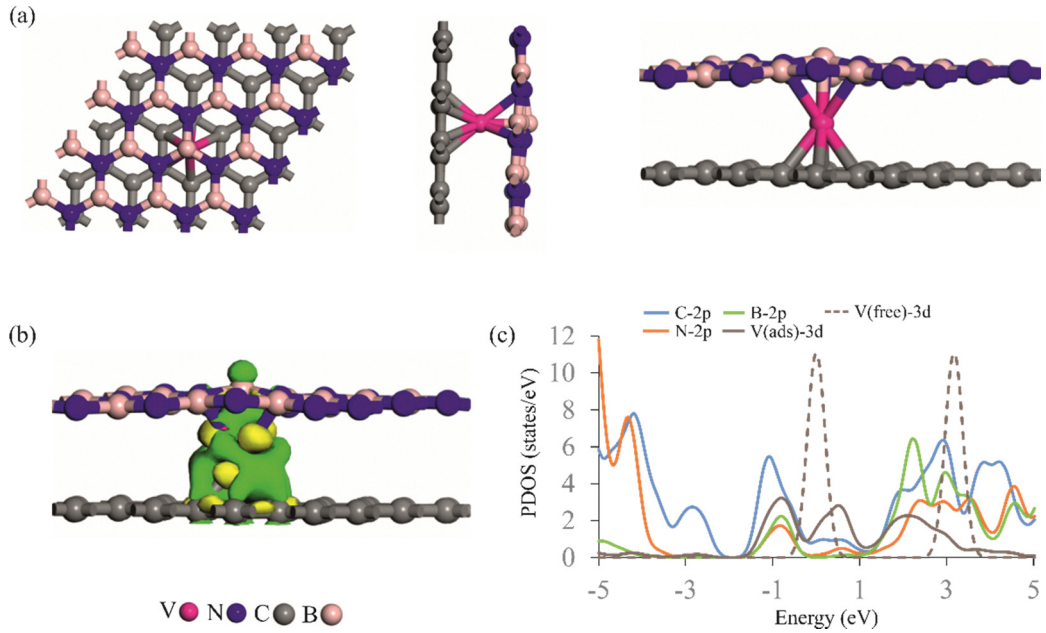

Fig. 1 (a) Optimized geometry of BN/V/Gr from top and side views, (b) the corresponding EDD map, and (c) PDOS graph. Charge gain and depletion regions in the EDD plots are shown in green and yellow, respectively. In the PDOS plots, the E = 0 indicates the Fermi level.

atom adjacent to V acquires some sp^3-like hybridization, which can aid this atom in adsorbing gas molecules.[71] According to Hirshfeld analysis, the V atom in the BN/V/Gr structure has a positive charge of 0.28 $|e|$, indicating that it acts as an electron donor to the BN and/or graphene surfaces. In contrast, the B atom adjacent to the V atom is positively charged by 0.19 $|e|$. This charge is 0.08 $|e|$ lower than that of a B atom on the pure h-BN sheet, implying that the presence of the sandwiched V atom pushes electrons toward it. This neighboring B atom is therefore identified as the active catalytic center within the BN/V/Gr structure. Hirshfeld charge analysis also indicates that the hybrid BN/V/Gr structure could enhance the polarization of the V atom, potentially improving the selectivity and activity for NOER. The green regions observed in the electron density difference (EDD) map support the existence of strong chemical bonds between the V moiety and BN/Gr surfaces (Fig. 1b). There is also a small electron density increased region above the B atom directly attached to the V atom. This verifies that the V atom pushes some electron towards the B atom and makes this atom to interact with potential gas molecules. Furthermore, as shown in Fig. 1c, the PDOS plots indicate an effective hybridization between the V-3d electronic states and the N-2p and C-2p states near the Fermi level, confirming the formation of strong V–N and V–C chemical bonds. The interaction between the V atom and the graphene or h-BN causes the 3d states of the V atom to split around the Fermi level. The emergence of these states can enhance charge transfer between the V atom and graphene/h-BN surface. Additionally, the significant overlap between the V-3d and B-2p states at E = −1 eV indicates a considerable hybridization of these states, leading to the transfer of some electrons to the B atom adjacent to the V. This is further supported by the observed buildup of electron density over the B atom discussed above. Besides, the adsorption energy for the V atom in the BN/V/Gr structure is calculated to be as high as −8.9 eV. This significantly negative value indicates that the V atom is firmly positioned between the h-BN and graphene layers.

We conducted AIMD simulations at a temperature of 500 K for a total duration of 2 ps and a time step of 1 fs. The final structure resulting from these simulations, along with the corresponding potential energy *versus* time trajectories, is shown in Fig. S1 of the SI. The results indicate that the binding distances between the V atom and its neighboring C, N, or B atoms, as well as the bond angles, exhibit minimal variation throughout the simulation period. Additionally, the potential energy of the system changes only slightly over time, suggesting that the BN/V/Gr structure maintains its integrity even at high temperatures. Therefore, the BN/V/Gr system is thermodynamically stable enough for further applications.

3.2. Addition of NO over BN/V/Gr

The adsorption of the NO molecule onto the BN/V/Gr is a crucial step in initiating the NOER process, similar to other catalytic reactions.[78,79] Therefore, a comprehensive evaluation of the most energetically favored configurations of a NO molecule on the BN/V/Gr surface was conducted. The relaxed structures, along with the PDOS plots and EDD maps, are shown in Fig. 2.

To determine if the NO molecule is stably attached to the substrate, we provide the values for adsorption energies (E_{ads}), changes in Gibbs free energy (ΔG), and net charge transfer (q_{CT}) in Table 1. The calculations show that NO can be added over the B atom in two different configurations, either through its nitrogen (N-end) or its oxygen (O-end) (see Fig. 2). The NO

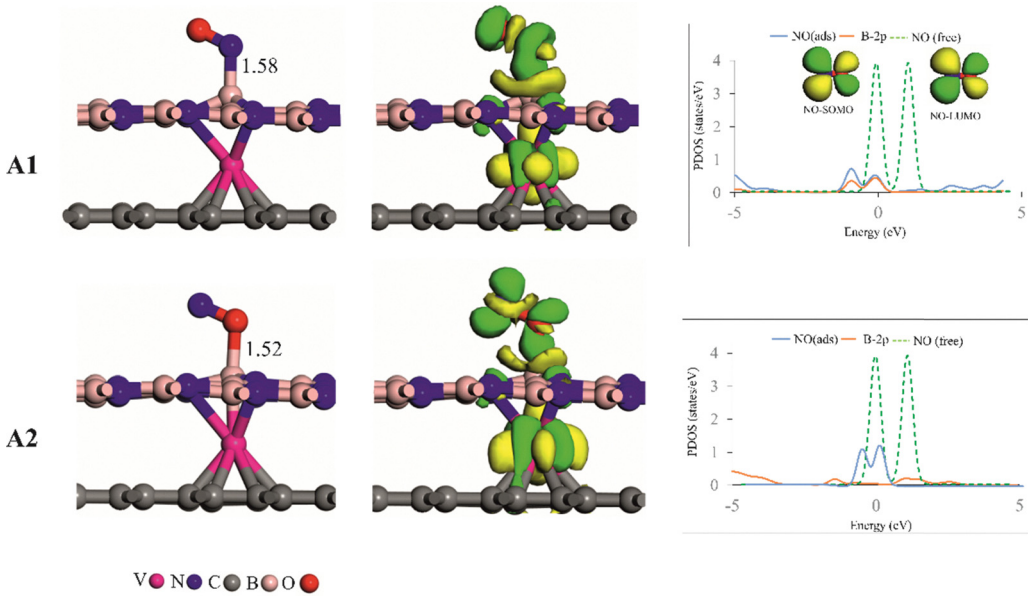

Fig. 2 The most stable geometries and binding distances (in Å) of the adsorbed NO molecule (structures **A1** and **A2**), and related EDD and PDOS plots. The charge gain and depletion regions in the EDD plots are shown in green and yellow, respectively. In the PDOS plots, the E = 0 indicates the Fermi level.

Table 1 Adsorption energy, charge shift, and Gibbs free energy change of complexes **A1** and **A2**[a]

Complex	E_{ads} (eV)	q_{CT} (e)	ΔG (eV)
A1	−1.95	0.27	−0.85
A2	−1.52	0.23	−0.69

[a] ΔG values at T = 298 K and P = 1 atm.

molecule in these configurations is oriented on the B atom, with a binding distance of 1.58 and 1.52 Å, respectively. These stable configurations resemble those achieved with other catalysts.[80–84] The E_{ads} value for the NO molecule when attached through its N-end (structure **A1**) is −1.95 eV, which is more negative (by 0.43 eV) than that for the O-end (structure **A2**). This indicates that adsorption of the NO molecule *via* the N-end is more energetically favored compared to the O-end. A charge of 0.27 $|e|$ transfers from the catalyst to the NO molecule, leading to elongation of the N–O bond. This is supported by the calculated N–O bond lengths of 1.30 Å for structure **A1** and 1.24 Å for structure **A2**, both of which are greater than the bond distance of the isolated NO (1.16 Å). According to Fig. 2, the EDD maps show a notable increase in electron density over the NO molecule and a decrease around the B atom. Note that the extent of rearrangement in the electron density is strongly linked to the NO adsorption energies in **A1** and **A2** structures. The PDOS analysis of the **A1** and **A2** structures reveals significant overlap between the singly-occupied molecular orbital (SOMO) of NO, which exhibits a π^* character, and the partially-occupied B-2p states. Importantly, the orbital interactions in complex **A1** are more substantial than those in **A2**, which is consistent with the E_{ads} values. This difference can be attributed to the greater contribution of the nitrogen atom in the SOMO, as illustrated in Fig. 2. In the case of **A1**, it is clear that the SOMO of the NO molecule downshifts and nearly disappears after adsorption. Finally, Table 1 demonstrates that the binding of NO is thermodynamically favorable at ambient conditions, as reflected by the negative ΔG values.

An interesting question to consider is whether NO can diffuse between the h-BN and graphene surfaces to interact directly with the V atom. Figure S2 presents the optimized structure for this scenario. The results indicate that this structure is less stable than the **A1** and **A2** complexes. This instability can be attributed to the diffusion of the NO molecule into the BN/V/Gr system, which weakens the V–C, V–N, and V–B interactions and increases the distance between the h-BN and graphene layers. Therefore, it can be concluded that NO molecules are unlikely to diffuse into the BN/V/Gr system and directly interact with the V atom.

3.3. NOER mechanism

Previous investigations[52–54] indicate that the concentration of NO molecules is essential for identifying the most desirable reaction paths and the resulting products in the NOER process. At low concentrations of NO, the primary product formed is ammonia (NH_3), which suggests that this reaction pathway is preferred under these conditions. Conversely, when the concentration of NO is increased to high levels, N_2 becomes the predominant product, indicating a shift in the reaction dynamics. This shift suggests that higher NO coverage alters the reaction mechanisms and thermodynamic preferences. Consequently, the NOER is systematically studied across both low and high NO coverage scenarios to better understand these variations in product formation and to optimize the reaction conditions for desired outcomes.

3.3.1. NOER at low NO concentration. Following the confirmation of the activation of the NO molecule, potential

reaction mechanisms for its reduction were explored to evaluate the electrocatalytic activity of the BN/V/Gr system. In each step of hydrogenation, an H^+/e^- pair is successively introduced to the intermediate species, and then the geometry of the resulting structure is optimized. The reaction paths for the NO electrochemical conversion to NH_3 are presented in Fig. 3a. The active site on the B atom is marked by (*) for all species. Initially, an H^+/e^- pair hydrogenates the activated NO molecule (*NO). As can be seen, there are two potential hydrogenation reaction pathways, labeled R1 and R2, to assess the efficiency of the BN/V/Gr in the context of NOER. In pathway R1, the initial H^+/e^- combines with the O atom of the *NO, leading to the creation of the *NOH moiety. In pathway R2, the *NO molecule is converted into *HNO intermediate by introducing an H^+/e^- pair. Two pathways for hydrogenating *NOH and *HNO moieties are defined: R1-1 and R1-2 (for R1) and R2-1 and R2-2 (for R2), see Fig. 3a. The optimized structures of all reaction intermediates associated with the four routes are illustrated in Fig. 4.

3.3.1.1. R1-1 route. In the *NOH species, the N–O bond distance is measured to be 1.38 Å, which is 0.14 Å greater than that in the *NO moiety. Additionally, the bond length of *N–B is measured at 1.52 Å. Fig. 5 and 6 present the ΔG and ΔE values along with the associated diagrams. For the first step of hydrogenation, the ΔE value is negative (−0.35 eV), while the ΔG is positive by 0.03 eV, indicating that this reaction is almost favorable at ambient temperature.

During the subsequent step, the hydrogenation process targets the oxygen atom in *NOH, leading to the generation of H_2O. Simultaneously, the remaining *N species establishes a bond with the boron atom, resulting in a bond length of 1.48 Å for the *N–B interaction. The ΔG for this step is −0.24 eV, facilitating the breaking of the N–O bond and resulting a water molecule. The estimated ΔE for this process is 0.22 eV. Once the H_2O molecule detaches from the system, a third H^+/e^- is subsequently combined with the *N moiety. This reaction generates the *NH intermediate, a crucial step in the process. The value of ΔG for this step is −1.79 eV, whereas the calculated value of ΔE is −2.15 eV. In the following step, hydrogenation of the *NH group produces the intermediate moiety *NH_2, with a chemical bond of 1.49 Å with the B atom. The ΔG and ΔE values for this step are −1.93 eV and −2.35 eV, respectively. In the final step, the *NH_2 species reacts with another hydrogen atom to produce *NH_3, which exhibits a ΔG value of 0.17 eV. Moreover, the ΔE of the latter step is measured to be −0.26 eV. Lastly, the NH_3 molecule can detach from the B atom with a ΔG value of −0.69 eV. In an acidic environment, the transformation of NH_3 into NH_4^+ can occur rapidly because this process releases a significant amount of energy. The release of energy can help in the removal of NH_3 from the surface of the catalyst, effectively regenerating the clean catalyst surface and enabling the start of a new NOER cycle.

3.3.1.2. R1-2 route. Another H^+/e^- pair is added to the *NOH, resulting in the formation of the *HNOH intermediate. At this stage, the ΔE and ΔG values are −1.68 and −1.28 eV, respectively (see Fig. 4). The comparison of routes R1-1 and R1-2 reveals that, in contrast to *N formation, the generation of *HNOH is highly exothermic (−1.68 eV), indicating that *HNOH formation is more advantageous. During this step, the addition of a proton/electron pair causes the *N–B bond to elongate from 1.52 Å (in *NOH) to 1.54 Å. Introducing additional H^+/e^- to the *HNOH intermediate results in H_2O and *NH species. The calculated ΔG and ΔE values are negative for this process (−0.75 and −0.25 eV). Subsequently, another H^+/e^- is added to *NH, leading to the formation of the *NH_2 species, which is energetically desirable, with a ΔG of −1.93 eV. The addition results in a further extension of the N–B bond by

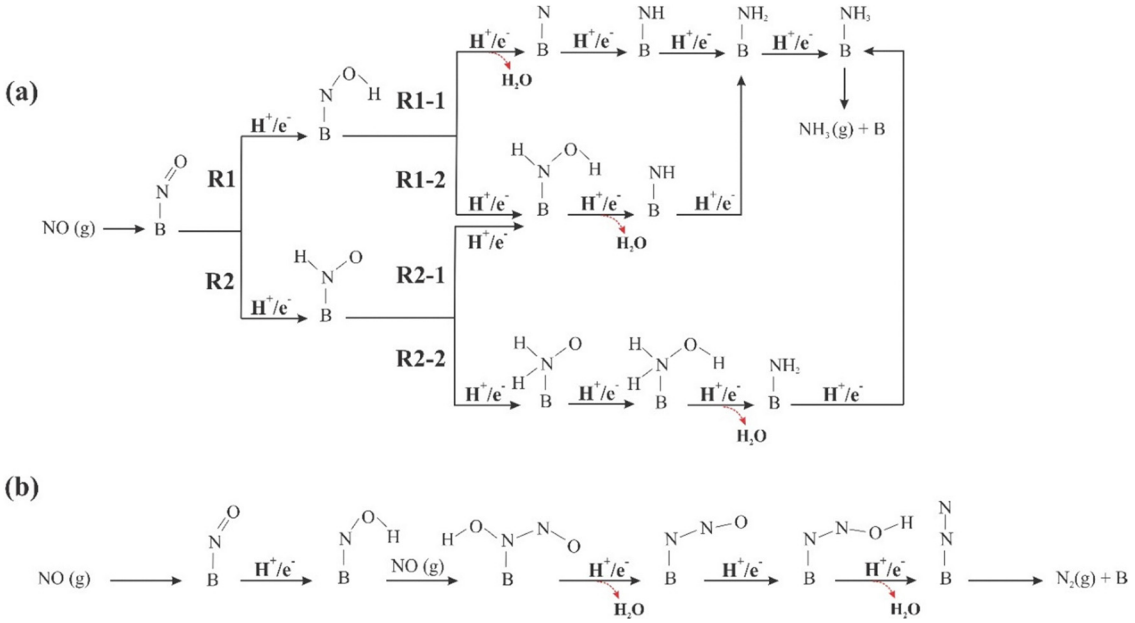

Fig. 3 Possible reaction routes for the NOER (within an acidic environment) under (a) low and (b) high surface concentration.

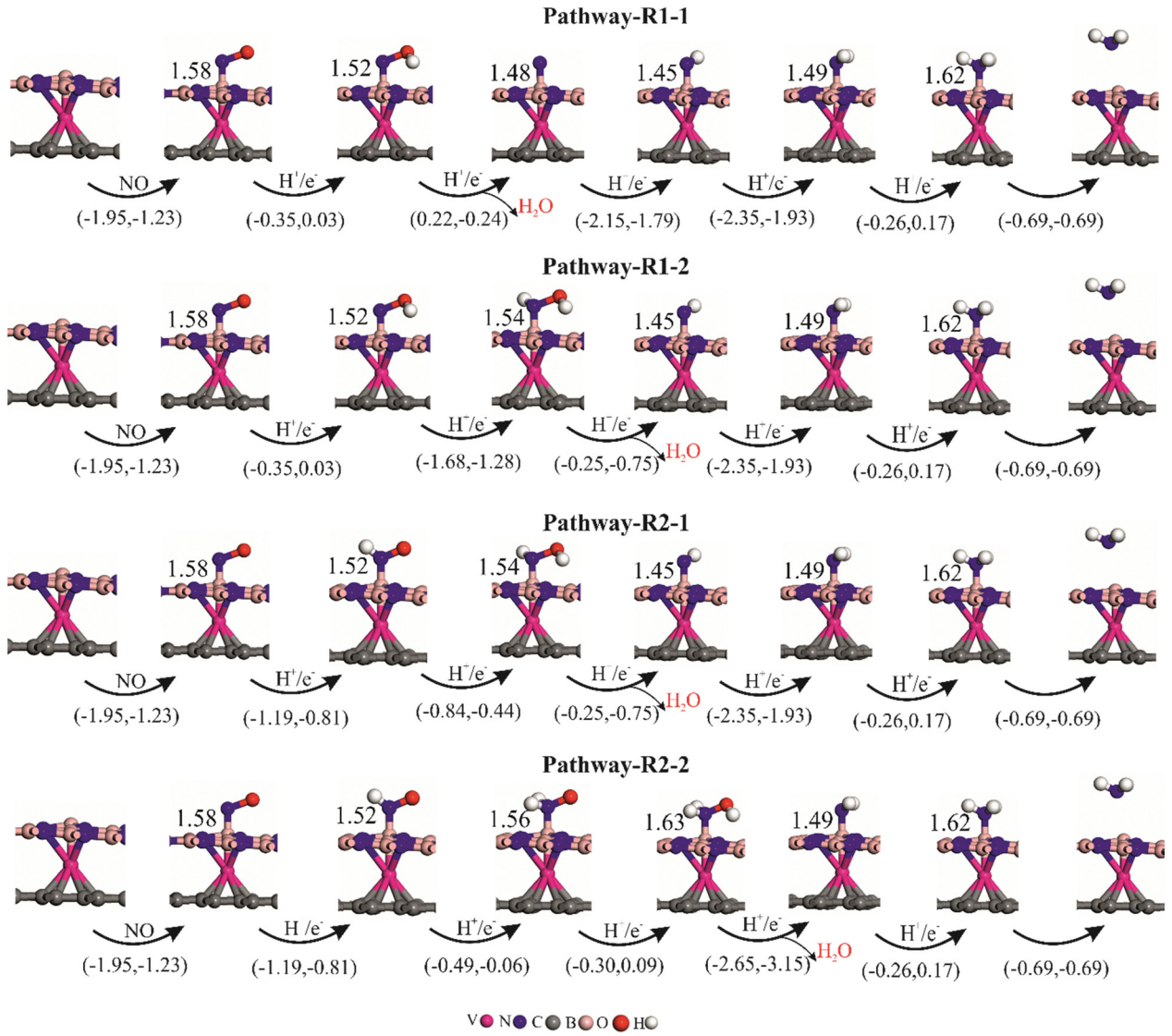

Fig. 4 Different NOER routes (within an acidic environment and at low NO coverage) over BN/V/Gr, along with the optimized intermediates (bond lengths in Å). The values within the parentheses are the related ΔE and ΔG, respectively.

0.04 Å. The ΔE for the formation of $*NH_2$ is −2.35 eV. As seen in Fig. 3a, the hydrogenation process follows the R1-1 route, with the values for ΔG and ΔE staying the same.

Examining the free energy diagrams for R1-1 and R1-2 (refer to Fig. 5) reveals that the fifth step (formation of NH_3) is the potential limiting step for the entire reaction, with a ΔG_{max} value of 0.17 eV. This value is substantially lower than those of Si–N_4 (0.56 eV),[82] B_4-decorated g-C_3N_4 (0.29 eV),[84] B-incorporated graphene (0.35 eV),[85] B-doped C_{60} fullerene (0.30 eV)[79] and Cu-decorated g-C_3N_4 (0.37 eV).[86] Also, the calculated ΔG_{max} value in the present study is comparable with that reported for the V-supported VS_2 (0.29 eV).[87]

3.3.1.3. R2-1 route. When NO is reduced *via* route R2, the *HNO species is obtained at the boron atom by adding an H^+/e^- pair to the nitrogen atom of *NO. The resulting *HNO has *N–B and N–O bond distances of 1.52 Å and 1.30 Å, respectively. These values are similar to those of *N–B (1.52 Å) and N–O (1.38 Å) in *NOH. Both ΔG and ΔE for this step are negative, indicating that the production of *HNO is thermodynamically more desirable than that of *NOH. Therefore, *HNO is essential to the NOER (see Fig. 5). The hydrogenation of the *HNO intermediate can occur through either its oxygen or nitrogen atom, allowing the NOER to proceed *via* two distinct routes, R2-1 and R2-2, as depicted in Fig. 3.

The electrochemical reduction of NO involves hydrogenation of the oxygen atom in *HNO *via* the R2-1 path, resulting in *HNOH, with a ΔG value of −0.44 eV. The related ΔE for this step is −0.84 eV. The bond distances for *N–B and N–O are approximately 1.54 Å and 1.47 Å, respectively. As the reaction continues and progresses to step 3, further hydrogenation of the oxygen atom occurs, resulting the H_2O molecule. This step results in an energy release of 0.25 eV, while the G value of the system decreases by 0.75 eV. By successively hydrogenating the

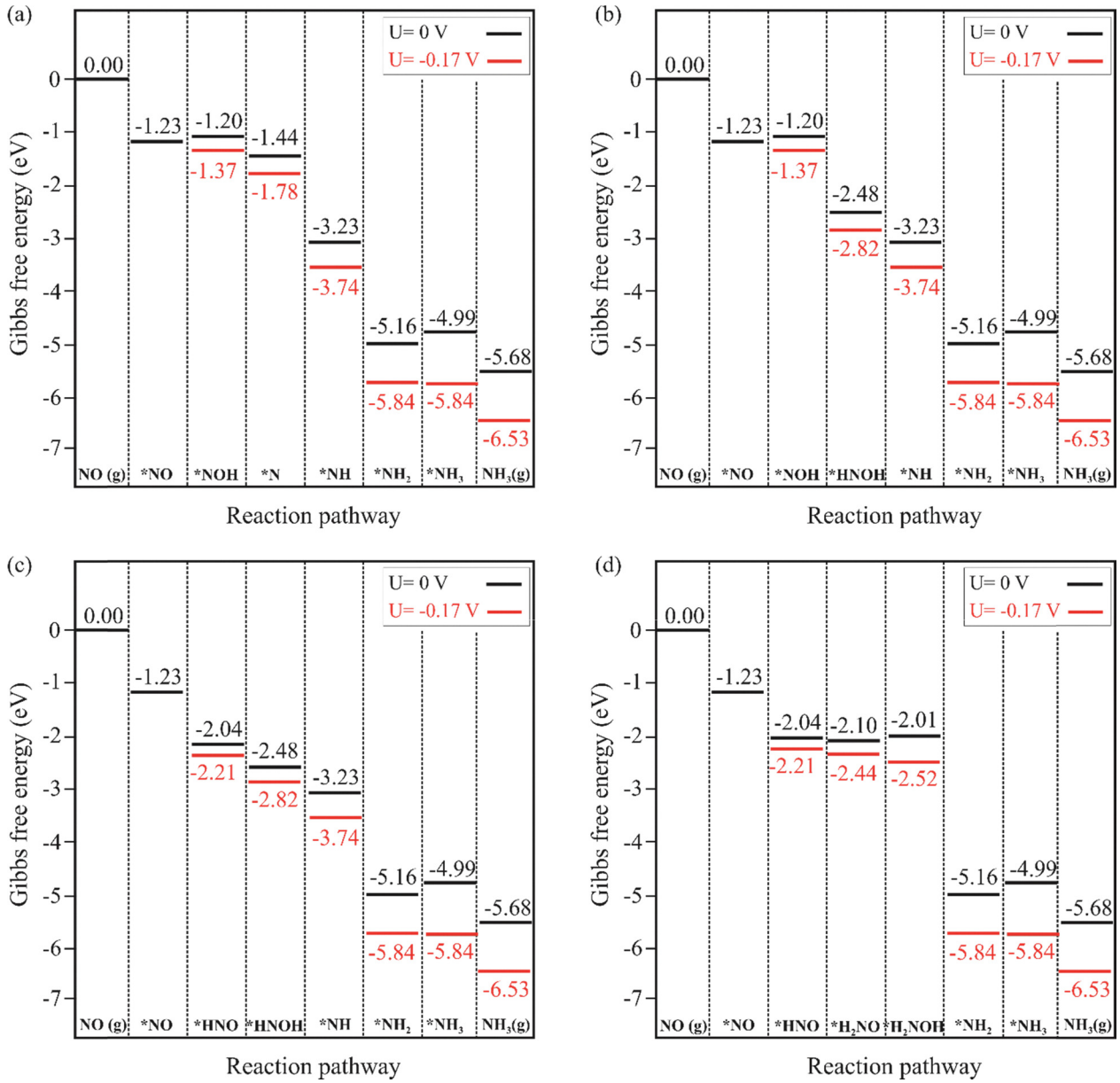

Fig. 5 Variation in the Gibbs free energy (ΔG) for the NOER into NH_3 within an acidic environment through different routes (low surface coverage): (a) R1-1, (b) R1-2. (c) R2-1, and (d) R2-2.

remaining *NH moiety, the NH_3 molecule is ultimately produced. These processes mirror those of route R1-2. The processes involved are the same as those related to route R1-2. The related ΔG and ΔE values are presented in Fig. 5 and 6.

3.3.1.4. R2-2 route. As the reduction process takes the R2-2 route, the second H^+/e^- adds to the N atom of *HNO, yielding the *H_2NO intermediate. The ΔE and ΔG for the formation of *H_2NO (−0.49 and −0.06 eV) are less negative compared to those for the formation of *HNOH (−0.84 and −0.44 eV). Thus, generating *HNOH is more desirable. Following that, the hydrogenation of *H_2NO yields the *H_2NOH moiety, with a ΔG of 0.09 eV, and an exothermic reaction energy (ΔE) of −0.30 eV. Adding another proton/electron pair to *H_2NOH may produce *NH_2 and H_2O. This process is capable of releasing a substantial energy (2.65 eV), leading to a notable free energy change of −3.15 eV. Lastly, the hydrogenation of *NH_2 can generate the *NH_3 species, which exhibits ΔG and ΔE values that are similar to those of the three other pathways reported earlier.

From a thermodynamic standpoint, the reaction routes R2-1 and R2-2 are favored because the Gibbs free energy associated with the hydrogenation of *NO (to generate *HNO) is much lower than that of *NOH. A comparison of the free energy values obtained from the R2-1 and R2-2 pathways clearly indicates that the first route is more favored. This preference can be attributed to the more favorable formation of the *HNOH species (−0.44 eV) in the R2-1 pathway compared to

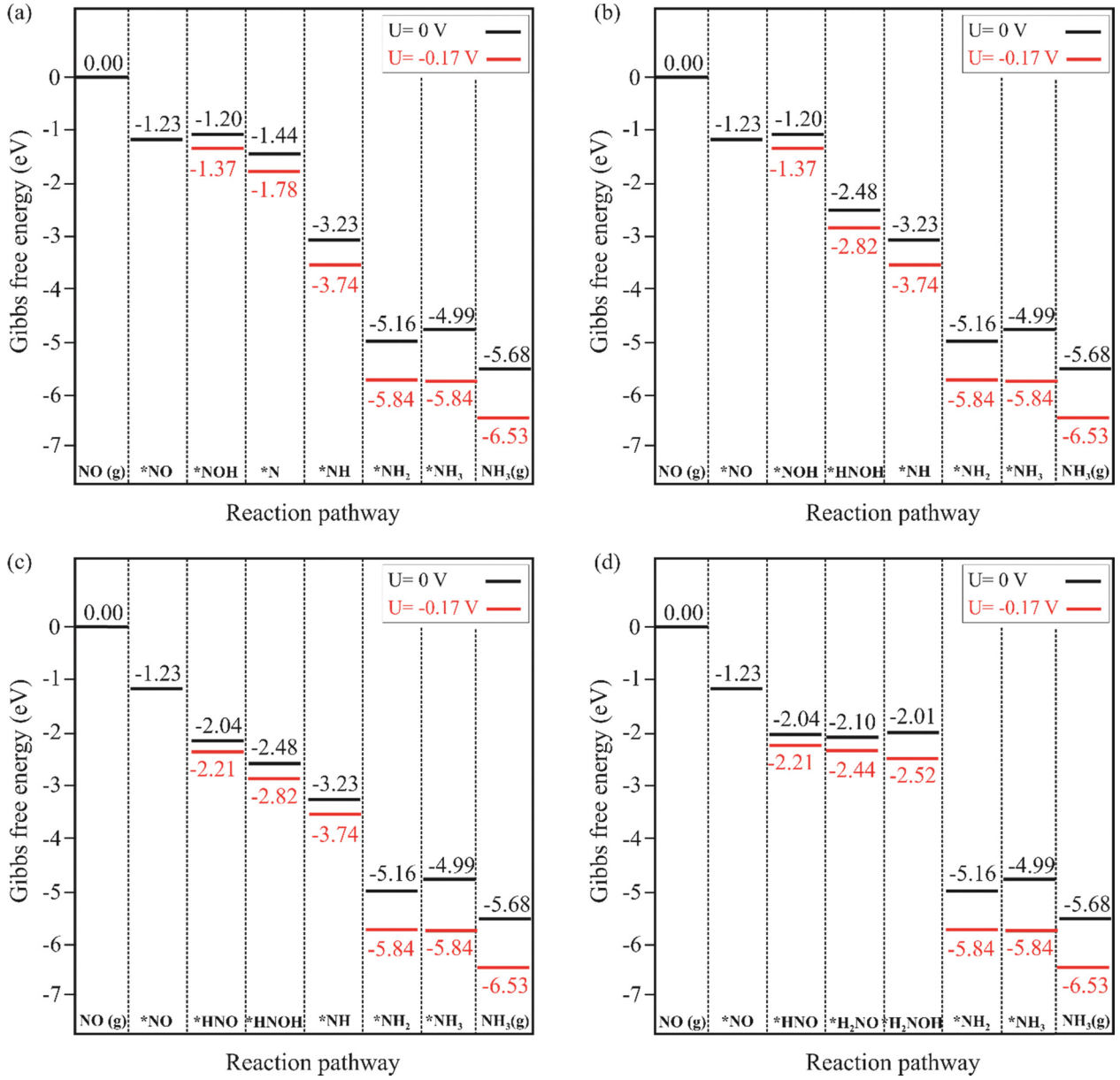

Fig. 6 Variation in the reaction energies (ΔE) for the NOER into NH_3 within an acidic environment through different routes (low surface coverage): (a) R1-1, (b) R1-2. (c) R2-1, and (d) R2-2.

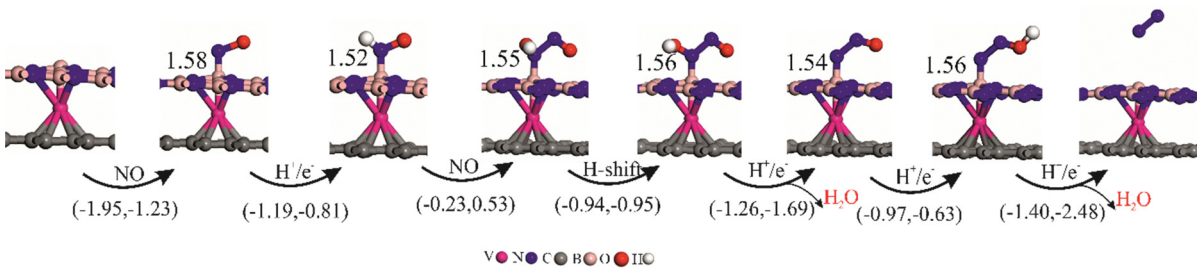

Fig. 7 Different NOER routes (at high NO concentration) over BN/V/Gr, along with the optimized intermediates (bond lengths in Å). The values within the parenthesis are the related ΔE and ΔG, respectively.

the R2-2 pathway (−0.06 eV). Hence, this study favors the R2-1 route for converting NO into NH_3.

3.3.2. NOER at high NO concentration. When the surface of examined catalyst is highly covered by NO molecules, the final product of the NOER shifts from NH_3 to N_2 (Fig. 3b). The relaxed structures, along with their corresponding ΔG and ΔE values, are illustrated in Fig. 7. The ΔG and ΔE profiles for the related reaction pathways are shown in Fig. 8. The interaction between the nitrogen atom of the *HNO species and the NO molecule generates *HNONO intermediate, with a free energy of 0.53 eV and a reaction energy of −0.23 eV. The bond length of the *N–B bond measures 1.56 Å, compared to 1.52 Å for the adsorbed *HNO, while the N–N bond distance reaches 1.88 Å.

Next, the hydrogen atom in the *HNONO species moves from the N atom to the O atom, resulting in the formation of *NOHNO with ΔE and ΔG values of −0.94 eV and −0.95 eV, respectively. The oxygen atom associated with the hydroxyl group in the *NOHNO intermediate is then hydrogenated, yielding H_2O and $*N_2O$ species. This step possesses a ΔG value of −1.69 eV and a ΔE of −1.26 eV. Further hydrogenation of the produced N_2O can lead to the formation of $*N_2OH$ and then to $*N_2 + H_2O$ species. The ΔG values for these last two steps are −0.63 eV and −2.48 eV, suggesting that the hydrogenation is energetically desirable and can take place at room temperature. Based on the ΔG values in Fig. 8, the formation of *HNONO is characterized as the potential-limiting step, with the highest free energy of 0.53 eV. This value is marginally greater than what has been reported for Si–N_4 doped graphene (0.45 eV)[55] and B-modified graphene (0.35 eV).[56]

3.4. The effect of pH

It is well-known that electrochemical reactions, such as the NOER[88] and ORR,[89] are sensitive to pH effects. However, these effects are not included in the COSMO approach and are challenging to address directly in DFT calculations. As mentioned earlier, pH effects can be corrected in the CHE method using the correction term $\Delta G_{pH} = k_B T \times pH \times \ln 10$. With an increase in the pH value, the energy associated with each proton and electron transfer step changes due to the impact of concentration on the free energy of H^+. At a pH of 1/4, the reaction free energies for *NOH and *HNO are calculated to be 0.09/0.27 eV and −0.38/−0.20 eV, respectively. This suggests that, after adjusting for the pH term in eqn (1), the formation of *HNO is still more favorable compared to *NOH. Note also that the total ΔG value for the formation of NH_3 remains negative even at higher pH values.

While the main goal of this study was to examine the NOER under acidic conditions, it is also important to briefly consider the possibility of this reaction occurring in an alkaline environment. In this context, the NOER is modeled by applying a negative charge to the adsorbed NO. The energy of an individual electron was considered to be zero because it is assumed that the electrons originate from the cathode rather than the solution. Additionally, the BN/V/Gr structure is a conductor capable of transferring charge with minimal energy loss. It is found that while a negative charge on the adsorbed NO results in a decrease in energy, this may facilitate the conversion of NO on the catalyst. However, energy barriers emerge in the following elementary reactions, *i.e.*, $NO^- + H_2O \rightarrow NOH + OH^-$, making the formation of NOH species very difficult. This a large barrier is understandable as it corresponds to the cleavage of O–H bond of H_2O and the desorption of the OH^- ion.

3.5. Competition of HER

To assess the selectivity of the proposed electrocatalysts, we also investigate the HER process over the BN/V/Gr catalyst. The

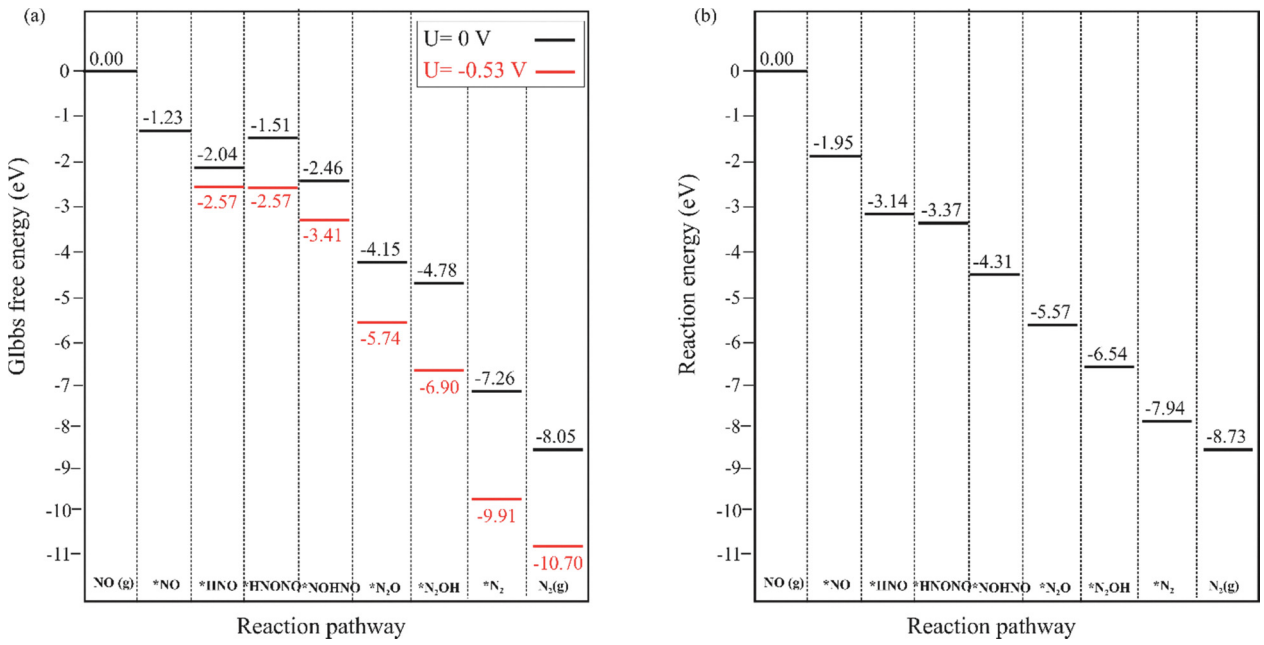

Fig. 8 Variation in the (a) ΔG, and (b) ΔE values for the NOER into N_2 within an acidic environment through different routes (high NO coverage).

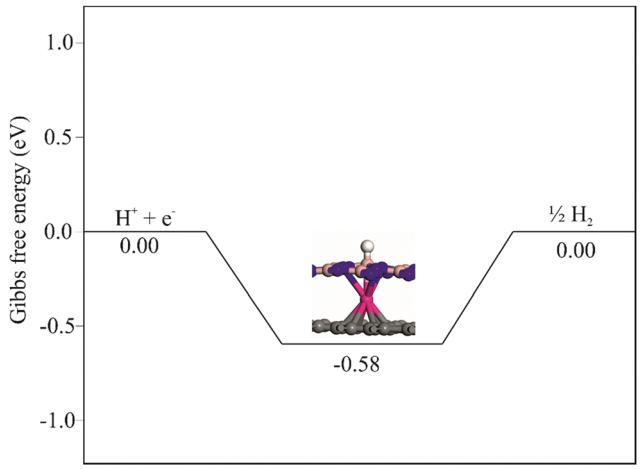

Fig. 9 ΔG diagram for the HER over BN/V/Gr.

HER takes place at the cathode as H^+ species are reduced, leading to the formation and release of H_2 molecules as described by the reaction $H^+ + e^- \rightarrow \frac{1}{2} H_2$. The ΔG diagram for the HER on the BN/V/Gr catalyst is presented in Fig. 9. An ideal catalyst for the HER exhibits a nearly zero free energy change ΔG(*H) for the hydrogen adsorption process. The calculated ΔG(*H) value for the BN/V/Gr system is −0.54 eV, indicating that the reaction is thermodynamically favorable at normal temperatures. This value closely matches the findings of Tang *et al.*[71] (−0.55 eV), indicating strong agreement between the results. However, since the NOER involves multiple protons and electrons and encompasses various intermediates, it presents kinetic challenges. As a result, most electrons and protons are likely to participate in the HER instead. Therefore, the selectivity of the electrocatalytic NOER could be achieved with the application of an appropriate external voltage. However, the adsorption energy E_{ads} for the hydrogen atom bonded to the B atom is obtained as −1.58 eV, which is notably less negative than that NO molecule (−1.95 eV). This indicates that the boron atom in BN/V/Gr has a stronger affinity for adsorbing NO compared to hydrogen. Consequently, besides having considerable catalytic performance, the electrocatalyst introduced in this study also shows selectivity for the NOER.

4. Conclusions

To summarize, the performance of the BN/V/Gr material was examined as an efficient electrocatalyst for the NOER, utilizing first-principles calculations. Polarization allows for the transfer of electronic charge from the V atom to the adjacent B atom in the h-BN layer, which can function as an active center to interact with a NO molecule *via* a donor–acceptor mechanism. The evaluated Gibbs free energies revealed that *HNO is one of the primary species at low coverages of NO molecules, while NH_3 emerges as the major product with a low limiting potential of 0.17 eV. Additionally, the effective combination of *HNO and NO species can result in the generation of N_2, with a limiting potential of 0.53 eV. Therefore, the NOER on BN/V/Gr thermodynamically favors the formation of NH_3. Moreover, the obtained adsorption energies and Gibbs free energies indicated that the HER may compete with the NOER on the BN/V/Gr structure; however, selectivity for the electrocatalytic NOER could be achieved with the application of an appropriate external voltage. Considering various parameters such as stability, noble metal-free, superior catalytic performance, selectivity *versus* HER, and good overall performance, BN/V/Gr may be an ideal choice for NOER. The results of this study may encourage additional research into the design and manufacture of effective electrocatalysts for eliminating poisonous NO molecules from the atmosphere.

Conflicts of interest

There are no conflicts to declare.

Data availability

The authors confirm that the data supporting the findings of this study are available within the article and/or its supplementary materials (SI). Supplementary information is available. See DOI: **https://doi.org/10.1039/d5nj03499j**.

Acknowledgements

The authors extend their appreciation to the Deanship of Research and Graduate Studies at King Khalid University for funding this work through Large Research Project under grant number RGP2/269/46.

References

1 D. A. Vallero, *Fundamentals of Air Pollution*, Academic Press, 2025.
2 F. Yan, H. Chen, T. Chi, J. Lu, X. Shen, F. Xie and Z. Zhang, *Chem. Eng. J.*, 2025, **520**, 166450.
3 F. Javier Jimenez-Jimenez, H. Alonso-Navarro, M. Trinidad Herrero, E. García-Martín and J. A. G. Agúndez, *Cur. Med. Chem.*, 2016, **23**, 2666–2679.
4 G. Tripodi, M. Lombardo, S. Kerav, G. Aiello and S. Baldelli, *Nutrients*, 2025, **17**, 393.
5 A. Azargoonjahromi, *Nitric oxide*, 2023, **134**, 23–37.
6 J. Prakash, S. B. Agrawal and M. Agrawal, *J. Soil Sci. Plant Nutr.*, 2023, **23**, 398–419.
7 L. Wang, J. Jin, W. Li, C. Li, L. Zhu, Z. Zhou and L. Yuan, *Energy Environ. Sci.*, 2024, **17**(23), 9122–9133.
8 Y. Sun, Y. Zhu, T. Xin, X. Li, X. Zhou, G. Bai and R. Zhu, *Appl. Surf. Sci.*, 2025, **708**, 163768.
9 Z. Yang, Y. Zhou, H. Li, J. Lei, P. Bing, B. He and Y. Li, *Asian J. Org. Chem.*, 2022, **11**(1), e202100656.
10 D. Zhu, M. Li, Z. Wu, Y. Du, B. Luo, P. Huang and S. Wen, *Eur. J. Org. Chem.*, 2019, **2019**(28), 4566–4571.
11 X. Rao, Q. Si, T. Shi, X. Han and S. Ma, *Comput. Theor. Chem.*, 2021, **1194**, 113080.

12 P. Kumar, T. A. Al-Attas, J. Hu and M. G. Kibria, *ACS Nano*, 2022, **16**, 8557–8618.
13 N. V. Rao Nulakani, V. S. Kumar Choutipalli, K. L. Shuford and M. A. Ali, *Fuel*, 2026, **404**, 136336.
14 D. Liao, G. Tian, F. Xiaoyu, Z. Li, Y. Sun, W. Chang and C. Zhang, *ACS Catal.*, 2025, **15**(10), 8219–8229.
15 R. Li and W. Guo, *Phys. Chem. Chem. Phys.*, 2022, **24**, 13384–13398.
16 P. Shen, X. Li, Y. Luo, N. Zhang, X. Zhao and K. Chu, *Appl. Catal., B*, 2022, **316**, 121651.
17 M. S. Iqbal, Z.-B. Yao, Y.-K. Ruan, R. Iftikhar, L.-D. Hao, A. W. Robertson, S. M. Imran and Z.-Y. Sun, *Rare Met.*, 2023, **42**, 1075–1097.
18 R. Li, C. Wang, J. Zhang and W. Guo, *Nano Res.*, 2025, **18**, 94907212.
19 M. D. Esrafili, *ChemistrySelect*, 2018, **3**, 12072–12079.
20 K. Chen, Y. Zhang, J. Xiang, X. Zhao, X. Li and K. Chu, *ACS Energy Lett.*, 2023, **8**, 1281–1288.
21 H. Li, D. Wu, J. Wu, W. Lv, Z. Duan and D. Ma, *Nanoscale*, 2024, **16**, 7058–7067.
22 S. Zhu, Y. Zhang, W. Liu, D. Yang, G. Zhou and Z. Yang, *J. Phys. Chem. C*, 2025, **129**, 3522–3530.
23 X.-H. Zhang, S.-J. Liu, L. Tian, Q. Wan, A.-M. Hu and X.-F. Li, *Chem. Phys.*, 2021, **546**, 111140.
24 J. Deng, D. Deng and X. Bao, *Adv. Mater.*, 2017, **29**, 1606967.
25 Z. Wang, J. Zhao, J. Wang, C. R. Cabrera and Z. Chen, *J. Mater. Chem. A*, 2018, **6**, 7547–7556.
26 H. Li, H. Li, M. Du, E. Zhou, W. R. Leow and M. Liu, *Chem. Sci.*, 2025, **16**, 1506–1527.
27 M. D. Esrafili and N. Saeidi, *New J. Chem.*, 2017, **41**, 13149–13155.
28 Y. Lou, Y. Cai, W. Hu, L. Wang, Q. Dai, W. Zhan, Y. Guo, P. Hu, X.-M. Cao and J. Liu, *ACS Catal.*, 2020, **10**, 6094–6101.
29 J. Liu, J. Zhu, H. Xu and D. Cheng, *ACS Catal.*, 2024, **14**, 6952–6964.
30 C. Y. Hsu, H. Pallathadka, J. Gupta, H. Ma, H. H. Al-Shukri, A. Kareem, A. H. Zwamel and Y. F. Mustafa, *Phytother. Res.*, 2024, **38**, 4336–4350.
31 C.-Y. Hsu, S. A. Jasim, E. A. M. Saleh, K. H. Firoz, S. R. Jyothi, D. Shit, P. P. Nayak, A. S. Chauhan, D. S. Obaida and A. Hashemzadeh, *Int. J. Biol. Macromol.*, 2025, **315**, 144475.
32 K. Xu, Q. Li, L. Xie, Z. Shi, G. Su, D. Harper, Z. Tang, J. Zhou, G. Du and S. Wang, *Ind. Crops Prod.*, 2022, **179**, 114661.
33 Y. Wei, Z. Gao, Y. Zhao, Z. Liang, Y. Zeng, Z. Li, F. Wu, C. Chen, Y. Peng and J. Dai, *IEEE Electron Device Lett.*, 2025, DOI: **10.1109/LED.2025.3608875**.
34 J. Xiong, Q. Hu, J. Wu, Z. Jia, S. Ge, Y. Cao, J. Zhou, Y. Wang, J. Yan and L. Xie, *Adv. Compos. Hybrid Mater.*, 2023, **6**, 99.
35 K. Zhang, C. Zhu, L. Xie, L. Zhang, X. Chai, C. Wu, S. Wang, W. Peng, G. Du and K. Xu, *Carbohydr. Polym.*, 2025, **359**, 123574.
36 R. Luo, K. Zhang, Y. Qin, L. Xie, X. Chai, L. Zhang, G. Du, S. Ge, M. Rezakazemi and T. M. Aminabhavi, *Chem. Eng. J.*, 2024, **480**, 148077.
37 G. Su, J. Xiong, Q. Li, S. Luo, Y. Zhang, T. Zhong, D. P. Harper, Z. Tang, L. Xie and X. Chai, *Chem. Eng. J.*, 2023, **455**, 140686.
38 J. Xiong, Y. Wang, H. Wang, L. Xie, X. Chai, L. Zhang, W. Peng, S. Wang, G. Du and K. Xu, *Ind. Crops Prod.*, 2024, **222**, 119769.
39 A. B. Ali, S. W. Ghori, M. Diab, R. MM, S. Ray, K. Chennakesavulu, R. Sharma, A. Abdullaev, M. Latipova and R. Siddikov, *Solid State Sci.*, 2025, **169**, 108070.
40 A. B. M. Ali, A. Y. Ahmed, G. P. Priya, S. Ray, P. Amrita, R. Sharma, S. Usanov, D. Jumanazarov, B. Madaminov, P. D. Jangir and S. Obaidur Rab, *J. Mol. Graphics Modell.*, 2026, **142**, 109194.
41 O. A. Khadhair, A. Y. Ahmed, G. P. Priya, S. Ray, A. Pal, V. Arora, O. Mukhitdinov, L. Safarova, D. P. Rao, A. Smerat and S. O. Rab, *Microchem. J.*, 2025, **219**, 115823.
42 L. Boldrin, F. Scarpa, R. Chowdhury and S. Adhikari, *Nanotechnology*, 2011, **22**, 505702.
43 S. M. Kim, A. Hsu, M. H. Park, S. H. Chae, S. J. Yun, J. S. Lee, D.-H. Cho, W. Fang, C. Lee and T. Palacios, *Nat. Commun.*, 2015, **6**, 8662.
44 T. T. Tran, K. Bray, M. J. Ford, M. Toth and I. Aharonovich, *Nat. Nanotechnol.*, 2016, **11**, 37–41.
45 S. Roy, X. Zhang, A. B. Puthirath, A. Meiyazhagan, S. Bhattacharyya, M. M. Rahman, G. Babu, S. Susarla, S. K. Saju and M. K. Tran, *Adv. Mater.*, 2021, **33**, 2101589.
46 L. Ben Said, N. H. Alrasheedi, A. B. M. Ali, M. Shaban, A. A. Hussein, H. Rajab, W. Rajhi and K. Hajlaoui, *J. Mec. Theor. Appl.*, 2026, **116**, 105902.
47 S. Moon, J. Kim, J. Park, S. Im, J. Kim, I. Hwang and J. K. Kim, *Adv. Mater.*, 2023, **35**, 2204161.
48 H. Fu, K. Huang, G. Yang, Y. Cao, H. Wang, F. Peng, X. Cai, H. Gao, Y. Liao and H. Yu, *ACS Catal.*, 2021, **11**, 8872–8880.
49 V. S. K. Choutipalli, K. Esackraj, E. Varathan and V. Subramanian, *Appl. Surf. Sci.*, 2022, **602**, 154406.
50 Y. Zhao, X. Xu, Q. Yuan, Y. Wu, K. Sun, B. Li, Z. Wang, A. Wang, H. Sun and M. Fan, *Mater. Horiz.*, 2023, **10**, 4930–4939.
51 X. Zhong, Y. K. Yap, R. Pandey and S. P. Karna, *Phys. Rev. B: Condens. Matter Mater. Phys.*, 2011, **83**, 193403.
52 J. G. Howalt, T. Bligaard, J. Rossmeisl and T. Vegge, *Phys. Chem. Chem. Phys.*, 2013, **15**, 7785–7795.
53 S. S. Meshkat, E. Ghasemy, A. Rashidi, O. Tavakoli and M. Esrafili, *Front. Environ. Sci. Eng.*, 2021, **15**, 109.
54 N. Kumar, S. Verma, P. Kumar, A. A. Khan, J. Park and V. C. Srivastava, *Carbon*, 2024, **218**, 118722.
55 X. Liao, R. Lu, L. Xia, Q. Liu, H. Wang, K. Zhao, Z. Wang and Y. Zhao, *Energy Environ. Mater.*, 2022, **5**, 157–185.
56 S.-C. Liu, X.-R. Zhu, D.-Y. Liu and D.-C. Fang, *Phys. Chem. Chem. Phys.*, 2023, **25**, 913–931.
57 R. Wu and L. Wang, *Phys. Chem. Chem. Phys.*, 2023, **25**, 2190–2202.
58 T. Demeyere and C.-K. Skylaris, *J. Phys. Chem. C*, 2024, **128**, 19586–19600.
59 Y. Qin, P. Li, Z. Li, T. Wu and Y. Su, *J. Phys. Chem. C*, 2023, **127**, 4934–4941.
60 K. Huang, L. Duan and J. Z. Zhang, *J. Chem. Theory Comput.*, 2024, **20**, 10961–10971.
61 S. Ringe, N. G. Hormann, H. Oberhofer and K. Reuter, *Chem. Rev.*, 2021, **122**, 10777–10820.
62 M. R. Dooley and S. Vyas, *Phys. Chem. Chem. Phys.*, 2025, **27**, 6867–6874.

63 J. Zhang, H. Zhang, T. Wu, Q. Wang and D. van der Spoel, *J. Chem. Theory Comput.*, 2017, **13**, 1034–1043.
64 A. V. Marenich, C. J. Cramer and D. G. Truhlar, *J. Chem. Theory Comput.*, 2008, **4**, 877–887.
65 A. Klamt and G. Schüürmann, *J. Chem. Soc., Perkin Trans.*, 1993, **2**, 799–805.
66 F. Wang, Y. Zhou, S. Lin, L. Yang, Z. Hu and D. Xie, *Nano Energy*, 2020, **78**, 105128.
67 P. Zhang, B. B. Xiao, X. L. Hou, Y. F. Zhu and Q. Jiang, *Sci. Rep.*, 2014, **4**, 3821.
68 P. Zhang, J. S. Lian and Q. Jiang, *Phys. Chem. Chem. Phys.*, 2012, **14**, 11715–11723.
69 Z. Xiu, W. Mu, X. Zhou and X. Han, *Chin. J. Catal.*, 2024, **65**, 126–137.
70 X. Chen, S. Lin and H. Zhang, *Renewable Energy*, 2022, **189**, 502–509.
71 S. Tang, Q. Dang, T. Liu, S. Zhang, Z. Zhou, X. Li, X. Wang, E. Sharman, Y. Luo and J. Jiang, *J. Am. Chem. Soc.*, 2020, **142**, 19308–19315.
72 J. P. Perdew, K. Burke and M. Ernzerhof, *Phys. Rev. Lett.*, 1996, **77**, 3865–3868.
73 B. Delley, *J. Chem. Phys.*, 2000, **113**, 7756–7764.
74 S. Grimme, *J. Comput. Chem.*, 2006, **27**, 1787–1799.
75 J. K. Nørskov, J. Rossmeisl, A. Logadottir, L. Lindqvist, J. R. Kitchin, T. Bligaard and H. Jonsson, *J. Phys. Chem. B*, 2004, **108**, 17886–17892.
76 M. Shao and Y. Shao, *J. Mater. Chem. A*, 2025, **13**, 22066–22073.
77 R. D. Johnson, 2006, **https://srdata.nist.gov/cccbdb**.
78 Y. Meng, Y. Gao, K. Li, H. Tang, Y. Wang and Z. Wu, *Appl. Surf. Sci.*, 2021, **542**, 148568.
79 N. Saeidi, M. D. Esrafili and J. J. Sardroodi, *RSC Adv.*, 2022, **12**, 3003–3012.
80 S. Ji and J.-X. Zhao, *New J. Chem.*, 2018, **42**, 16346–16353.
81 N. Saeidi, M. D. Esrafili and J. J. Sardroodi, *Appl. Surf. Sci.*, 2021, **544**, 148869.
82 N. Saeidi and M. D. Esrafili, *Int. J. Hydrogen Energy*, 2023, **48**, 19509–19521.
83 Z. Yin, Z. Wang, Y. Gao, Z. Wang, Z. Wei and H. Wang, *Mol. Catal.*, 2023, **550**, 113556.
84 N. Venkateswara Rao Nulakani, V. Surya Kumar Choutipalli and M. Akbar Ali, *Appl. Surf. Sci.*, 2025, **680**, 161470.
85 S. Ji and J. Zhao, *New J. Chem.*, 2018, **42**, 16346–16353.
86 Q. Wu, W. Wei, X. Lv, Y. Wang, B. Huang and Y. Dai, *J. Phys. Chem. C*, 2019, **123**, 31043–31049.
87 Y. Duan, D. Wu and Z. Qin, *Electrochim. Acta*, 2025, **538**, 146954.
88 D. Wang, X. F. Lu, D. Luan and X. W. Lou, *Adv. Mater.*, 2024, **36**, 2312645.
89 V. Monini, M. Bonechi, C. Bazzicalupi, A. Bianchi, P. Gentilesca, W. Giurlani, M. Innocenti, A. Meoli, G. M. Romano and M. Savastano, *Dalton Trans.*, 2024, **53**, 2487–2500.